An Improved Passivity-Based Direct Power Control Strategy for AC/DC Converter Under Unbalanced and Distorted Grid Conditions

Qicai Ren, Alian Chen, *Member, IEEE*, Jingyang Fang, *Senior Member, IEEE*, Xi Liu, Tong Liu, Guanguan Zhang, *Member, IEEE*, and Chenghui Zhang, *Fellow, IEEE*

***Abstract*—AC/DC power converter is the momentous interface of the power router, which is responsible for maintaining the dc bus voltage stability. However, under unbalanced and distorted grid voltage conditions, there are voltage ripples in the dc bus, and grid currents will also be severely distorted. Accordingly, this article proposes an improved passivity-based direct power control (IPBDPC) strategy based on extended reactive power theory in the $\alpha\beta$-axis, which can effectively suppress dc voltage ripples and current harmonics of power converter. Meanwhile, with the proposed IPBDPC, the fundamental grid voltages and those orthogonal components are injected into the improved passivity model, so that the controller can further reduce the THD of the grid current when unbalanced and distorted grid conditions coexist. Compared with the traditional modified direct power control, the IPBDPC strategy has a simple structure and strong robustness, does not require complex positive and negative sequence separation, and power compensation value calculation. Moreover, the sequence impedance model of IPBDPC is constructed based on the harmonic linearization method to verify the robustness of the control system against parameters uncertainty. The simulation and experimental results based on a three-phase three-level converter system further demonstrated the effectiveness of the proposed control strategy.**

***Index Terms*—AC/DC power converter, direct power control (DPC), passivity-based control (PBC), unbalanced and distorted grid voltage.**

I. Introduction

THE power router (PR) can provide flexible and standardized power electronic interfaces for all types of distributed energies, storage units, loads, and even power grids [1], and fulfil energy conversion, transmission, and routing [2], as shown in Fig. 1. Among them, the ac/dc converter, as the sole power interface between utility ac grid and PR, is responsible for maintaining the dc bus voltage stability and sinusoidal grid currents under ideal grid. However, the grid voltages are sometimes unbalanced or distorted [3], which are caused by the increasing penetration level of the renewable energy into power grid, grid faults and disturbances, and grid impedance unbalances [4], [5]. At this time, the traditional control strategies of converter are no longer applicable, the dc bus voltage ripples increase notably, and the total harmonic distortion (THD) of current deteriorates. Therefore, it is significant to develop the advanced control schemes to cope with this issue [6], [7]. Substantially, the advanced schemes of ac/dc converter are broadly classified into two categories, namely voltage-oriented control (VOC) and direct power control (DPC). VOC is a mature and popular scheme to realize current control in industrial applications, which uses proportional–integral (PI) controller and synchronous transformation. When the grid voltage was unbalanced, the double synchronous reference frame (DSRF)-based VOC control was a commonly used approach, which required sequence components extraction of the grid voltages and currents through DSRF and decoupling DSRF technologies [8], [9], [10]. Moreover, to enhance the robustness under the nonideal grids, the extension self-tuning filter [11] and multivariable filter [12] were designed against dc offset and distorted grid conditions. But complicated procedures for positive/negative sequence separation and more control parameters adjustment are required. To address this drawback, the proportional integral resonance (PIR) control has been proposed to reduce THD of grid current [13]. However, the VOC depends on the inner current loop, and it is difficult to take

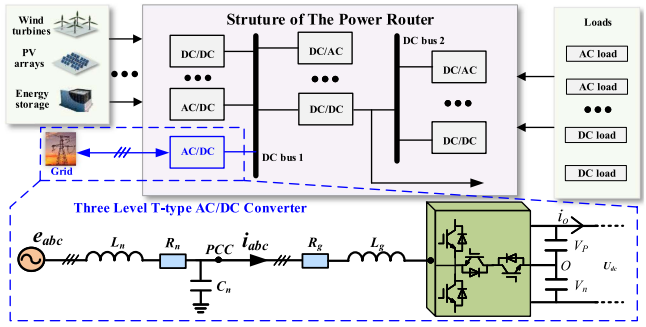

Fig. 1. PR structure and its grid-interface converter.

Manuscript received 13 February 2023; revised 27 April 2023 and 17 June 2023; accepted 29 June 2023. Date of publication 12 July 2023; date of current version 1 September 2023. This work was supported in part by the National Natural Science Foundation of China under Grant U2006222 and Grant 51877128, in part by National Key Research and Development Program of China under Grant 2022YFB2402900, in part by the Foundation for Innovative Research Groups of the National Natural Science Foundation of China under Grant 61821004, and in part by Major Scientific and Technological Innovation Project of Shandong Province 2019JZZY010904. Recommended for publication by Associate Editor J. Pou.

The authors are with the School of Control Science and Engineering, Shandong University, Jinan 250061, China (e-mail: qicairen@mail.sdu.edu.cn; chenalian@sdu.edu.cn; jingyangfang@sdu.edu.cn; liuxi_auto@163.com; liut6@163.com; dr_zgg@163.com; zchui@sdu.edu.cn).

Color versions of one or more figures in this article are available at https://doi.org/10.1109/TPEL.2023.3294806.

Digital Object Identifier 10.1109/TPEL.2023.3294806

into account the power oscillation caused by the unbalanced grid. Besides, the dynamic performance of VOC is severely limited by the bandwidth of current loop and phase-locked loop (PLL) [14].

In contrast to VOC, DPC eliminates the current regulator, and the reference voltage vector is directly obtained by the power control loop, with a very fast dynamic response [15], [16]. Recently, the control methods under unbalanced or distorted grid voltage conditions have also been extended to DPC. The PIR-based reference power compensation method with third-order harmonic [17], and model predictive direct power control (MPDPC) with different power compensation objectives [18], can eliminate current harmonics or power ripples. In [19], a DPC strategy based on multiorder harmonic control was proposed to suppress the THD of grid current under grid voltage distortion. However, the extraction of positive/negative sequence components and multiorder harmonic current components requires multiple notch filters or bandpass filters, which undoubtedly increases the control complexity. In addition, the calculation of the power compensation method is particularly complex. To address this problem, the extended reactive power theory was combined with deadbeat DPC [20] and MPDPC [21], [22], and no additional power compensation is required. The grid current distortion and active power oscillations can be automatically eliminated. However, the abovementioned control methods are computationally complex, and sensitive to parameter variations.

Recently, the application of passivity-based control (PBC) in power converter has attracted extensive attentions [23]. The PBC strategy is an energy-shaping method considering the energy dissipation of the system, and has clear physical meaning and simple structure [24]. It tracks the current or power references by injecting damping terms, resulting in solid robustness against external perturbations [25]. In order to enhance the robustness under model uncertainties, a hybrid control approach that includes a PI-based voltage loop and PBC current loop was proposed for the rectifier [26], [27], which will further improve the control ability of dc voltage [23]. But the abovementioned hybrid PBC methods are only applicable to ideal grid conditions. Recently, a PBC current control strategy with different power compensation objectives was proposed to reduce the active power and reactive power ripple when the grid voltage was unbalanced [28]. In [29], the hybrid passive control strategy embedded with negative-sequence grid voltage feedforward can suppress the imbalance of grid current. Moreover, the line voltage was taken as the state variable of the passivity-based model, which can realize the grid sinusoidal currents without extracting the negative-sequence components of the rectifier [30]. However, the aforementioned PBC methods are used in combination with VOC scheme, and the bandwidth of current loop and PLL limit the dynamic response of the converter. In addition, only unbalanced grid voltage conditions are considered, while the influence of distorted grid voltage conditions is ignored.

Motivated by the abovementioned inadequacies, this article develops an improved passivity-based direct power control (IPBDPC) strategy for three-level T-type ac/dc converter ($3LT^2C$) under unbalanced and distorted grid conditions. The major contributions of this article are as follows.

1) The passivity-based Euler Lagrange (EL) model for direct power controller is rebuilt by introducing the extended reactive power theory, which effectively suppresses the active power oscillations and current harmonics of the $3LT^2C$ under unbalanced grid conditions. Then, the fundamental-frequency grid voltages and their orthogonal components are injected into the improved passivity model, so the improved control strategy can still reduce the THD of the grid currents when unbalanced and distorted grid conditions coexist.
2) The sequence-impedance model of IPBDPC strategy for $3LT^2C$ is designed based on the harmonic linearization method in the $\alpha\beta$ axis. The robustness and stability, and parameters tuning methods of the converter, are investigated based on Nyquist criterion and frequency response analysis of impedance.

The rest of this article is organized as follows. The modeling and proposed IPBDPC strategy for $3LT^2C$ are given in Section II. Section III discusses the robustness of IPBDPC based on the proposed sequence-impedance model. The feasibility of the control scheme is verified by simulation and experiments given in Section IV. Finally, Section V concludes this article.

II. Modeling of Grid-Connected Rectifier and the Proposed IPBDPC Control Method

Compared with two-level converter, the three-level topologies have better harmonic characteristics and lower voltage stress of power devices. Among them, the $3LT^2C$ topology has higher efficiency for medium switching frequencies (8–24 kHz), making it the most competitive converter topology in low-voltage applications [31]. Therefore, this study takes a three-phase $3LT^2C$ connected to a grid through an L-filter as the object, as shown in Fig. 1.

A. Modeling Analysis

$$L_g \frac{di_{\alpha\beta}}{dt} = e_{\alpha\beta} - R_g i_{\alpha\beta} - u_{\alpha\beta} \tag{1}$$

where $i_{\alpha\beta}$, $e_{\alpha\beta}$, and $u_{\alpha\beta}$ indicate the stationary reference frame components of the grid currents i_{abc}, grid voltages e_{abc}, and converter voltage vectors, respectively. L_g and R_g are the filter inductance and resistance, respectively. According to instantaneous power theory (IPT), the active power P_g and reactive power Q_g on the grid side are calculated as

$$\begin{cases} P_g = 1.5Re(i^*_{\alpha\beta} e_{\alpha\beta}) \\ Q_g = 1.5Im(i^*_{\alpha\beta} e_{\alpha\beta}) \end{cases} \tag{2}$$

where "$*$" indicates the conjugate of a complex vector. For unbalanced grid voltage conditions, the extended reactive power theory (ERPT) can better represent the instantaneous reactive power change than the Q_g [20], which is expressed as

$$Q_g^{\text{ext}} = 1.5Re\left(i^*_{\alpha\beta} e'_{\alpha\beta}\right) \tag{3}$$

where $e'_{\alpha\beta}$ denotes their quadrature values that lag $e_{\alpha\beta}$ by 90 electrical degrees. The $3LT^2C$ is a three-phase three-wire system with no zero sequence path, so the grid currents only contain positive-sequence and negative-sequence components when the grid voltages are unbalanced. At this time, the active and reactive

power can be expressed as

$$\begin{cases} P_{\mathrm{g}} = P_{\mathrm{g0}} + P_{\mathrm{gc2}} + P_{\mathrm{gs2}} \\ Q_{\mathrm{g}} = Q_{\mathrm{g0}} + Q_{\mathrm{gc2}} + Q_{\mathrm{gs2}} \\ Q_g^{\mathrm{ext}} = Q_{g0}^{\mathrm{ext}} + Q_{gc2}^{\mathrm{ext}} + Q_{gs2}^{\mathrm{ext}} \end{cases} \tag{4}$$

$$\begin{cases} P_{\mathrm{gc2}} = 1.5\left(e_\alpha^+ i_\alpha^- + e_\beta^+ i_\beta^-\right) \\ \qquad = 1.5\left|U_{\mathrm{g}}^+\right|\left|I_{\mathrm{g}}^-\right|\cos\left(2\omega_f t + \theta_u^+ - \theta_i^-\right) \\ P_{\mathrm{gs2}} = 1.5\left(e_\alpha^- i_\alpha^+ + e_\beta^- i_\beta^+\right) \\ \qquad = 1.5\left|U_{\mathrm{g}}^-\right|\left|I_{\mathrm{g}}^+\right|\cos\left(2\omega_f t + \theta_i^+ - \theta_u^-\right) \end{cases} \tag{5}$$

$$\begin{cases} Q_{\mathrm{gc2}} = 1.5\left(e_\beta^+ i_\alpha^- - e_\alpha^+ i_\beta^-\right) \\ \qquad = 1.5\left|U_{\mathrm{g}}^+\right|\left|I_{\mathrm{g}}^-\right|\sin\left(2\omega_f t + \theta_u^+ - \theta_i^-\right) \\ Q_{\mathrm{gs2}} = 1.5\left(e_\beta^- i_\alpha^+ - e_\alpha^- i_\beta^+\right) \\ \qquad = -1.5\left|U_{\mathrm{g}}^-\right|\left|I_{\mathrm{g}}^+\right|\sin\left(2\omega_f t + \theta_i^+ - \theta_u^-\right) \end{cases} \tag{6}$$

$$\begin{cases} Q_{gc2}^{\mathrm{ext}} = 1.5\left(e_\alpha'^+ i_\alpha^- + u_\beta'^+ i_\beta^-\right) \\ \qquad 1.5\left|U_{\mathrm{g}}^+\right|\left|I_{\mathrm{g}}^-\right|\sin\left(2\omega_f t + \theta_u^+ - \theta_i^-\right) \\ Q_{gs2}^{\mathrm{ext}} = 1.5\left(e_\alpha'^- i_\alpha^+ + e_\beta'^- i_\beta^+\right) \\ \qquad 1.5\left|U_{\mathrm{g}}^-\right|\left|I_{\mathrm{g}}^+\right|\sin\left(2\omega_f t + \theta_i^+ - \theta_u^-\right) \end{cases} \tag{7}$$

where P_{g0}, Q_{g0}, and Q_{g0}^{ext} are the dc components of P_g, Q_g, and Q_g^{ext}, respectively. Others are the second-order harmonic ac components caused by negative-sequence voltage and current. $e_{\alpha\beta}^+$, $e_{\alpha\beta}^-$, $i_{\alpha\beta}^+$, and $i_{\alpha\beta}^-$ are positive and negative sequence components of grid voltage and current, respectively, $|U_g^+|$, $|I_g^+|$, $|U_g^-|$, and $|I_g^-|$ are the positive and negative sequence component amplitudes of grid voltage and current, respectively, θ_i^+, θ_u^+, θ_i^-, and θ_u^- are the initial phase of the positive and negative sequence component of grid voltage and current, respectively. ω_f is the fundamental frequency.

To achieve stable active power and sinusoidal current, the following equation needs to be met:

$$\begin{cases} P_{gc2} + P_{gs2} = 0 \\ Q_{gc2}^{\mathrm{ext}} + Q_{gs2}^{\mathrm{ext}} = 0. \end{cases} \tag{8}$$

Therefore, if the fluctuations of active power P_g can be eliminated, the fluctuations of Q_{gc2}^{ext} can also be eliminated at the same time. Besides, when the grid voltage is balanced, the grid voltages and those quadrature components meet the following relationship:

$$e_\alpha' = e_\beta, e_\beta' = -e_\alpha. \tag{9}$$

At this time, $Q_g^{\mathrm{ext}} = Q_g$ can be obtained, so the novel power theory combination is also applicable to balanced grid voltage.

Then, the dynamic equation of P_g and Q_g^{ext} can be obtained by taking the derivative of (2) and (3), given by

$$\begin{cases} \frac{dP_g}{dt} = 1.5\left(e_\alpha \frac{di_\alpha}{dt} + i_\alpha \frac{de_\alpha}{dt} + e_\beta \frac{di_\beta}{dt} + i_\beta \frac{de_\beta}{dt}\right) \\ \frac{dQ_g^{\mathrm{ext}}}{dt} = 1.5\left(e_\alpha' \frac{di_\alpha}{dt} + i_\alpha \frac{de_\alpha'}{dt} + e_\beta' \frac{di_\beta}{dt} + i_\beta \frac{de_\beta'}{dt}\right). \end{cases} \tag{10}$$

And the dynamic equation of e_α, e_β, e_α', and e_β' can satisfy the following formula:

$$\begin{cases} \frac{de_\alpha}{dt} = -\omega_f e_\alpha', \frac{de_\beta}{dt} = -\omega_f e_\beta' \\ \frac{de_\alpha'}{dt} = -\omega_f e_\alpha, \frac{de_\beta'}{dt} = \omega_f e_\beta. \end{cases} \tag{11}$$

Substituting (1) and (11) into (10), the dynamic model of the active and reactive power can be given by

$$\begin{cases} \frac{2}{3}L\frac{dP_g}{dt} = e_\alpha^2 + e_\beta^2 - (e_\alpha u_\alpha + e_\beta u_\beta) - \frac{2}{3}R_g P_g \\ \qquad\qquad - \frac{2}{3}\omega_f L_g Q_g^{\mathrm{ext}} \\ \frac{2}{3}L\frac{dQ_g^{\mathrm{ext}}}{dt} = e_\alpha' e_\alpha + e_\beta' e_\beta - (e_\alpha' u_\alpha + e_\beta' u_\beta) - \frac{2}{3}R_g Q_g^{\mathrm{ext}} \\ \qquad\qquad + \frac{2}{3}\omega_f L_g P_g. \end{cases} \tag{12}$$

From (12), we can obtain the EL model of the 3LT^{2}C, as follows:

$$\boldsymbol{M}\dot{\boldsymbol{x}} + \boldsymbol{J}\boldsymbol{x} + \boldsymbol{R}\boldsymbol{x} = \boldsymbol{u} \tag{13}$$

where $\boldsymbol{M}$ and $\boldsymbol{R}$ are a positive definite symmetric coefficient matrix, and $\boldsymbol{R}$ is the system dissipation term. $\boldsymbol{J}$ is an antisymmetric coefficient matrix and $\boldsymbol{J^T} = -\boldsymbol{J^T}$ [23], [24], [25]. $\boldsymbol{x}$ represents the state variable vector, $\boldsymbol{u}$ is the matrix of converter voltage vector, and

$$\begin{aligned} \boldsymbol{x} &= \begin{bmatrix} P_g \\ Q_g^{\mathrm{ext}} \end{bmatrix}, \boldsymbol{M} = \begin{bmatrix} \frac{2}{3}L_g & 0 \\ 0 & \frac{2}{3}L_g \end{bmatrix} \\ \boldsymbol{J} &= \begin{bmatrix} 0 & \frac{2}{3}\omega_f L_g \\ -\frac{2}{3}\omega_f L_g & 0 \end{bmatrix}, \boldsymbol{R} = \begin{bmatrix} \frac{2}{3}R_g & 0 \\ 0 & \frac{2}{3}R_g \end{bmatrix} \\ \boldsymbol{u} &= \begin{bmatrix} e_\alpha^2 + e_\beta^2 - (e_\alpha u_\alpha + e_\beta u_\beta) \\ e_\alpha' e_\alpha + e_\beta' e_\beta - (e_\alpha' u_\alpha + e_\beta' u_\beta) \end{bmatrix}. \end{aligned} \tag{14}$$

B. Instantaneous Power Loop Design

To track the power references, let error $\boldsymbol{x_e} = \boldsymbol{x_{\mathrm{ref}}} - \boldsymbol{x}$, and the error storage function is given by

$$\boldsymbol{H_e}(\boldsymbol{x}) = \frac{1}{2}\boldsymbol{x_e^T M x_e}. \tag{15}$$

Injecting damping $\boldsymbol{R_a}$ to the dissipation term can achieve $\boldsymbol{H_e}(\boldsymbol{x}) \to 0$ rapidly, which increases the convergence rate of $\boldsymbol{x} \to \boldsymbol{x_{\mathrm{ref}}}$. Therefore, the new dissipation term $\boldsymbol{R_d}$ is

$$\boldsymbol{R_d x_e} = (\boldsymbol{R} + \boldsymbol{R_a})\boldsymbol{x_e} \tag{16}$$

where the additional damping matrix R_a is a positive definite symmetric matrix, as well as R

$$\boldsymbol{R_a} = \begin{bmatrix} r_a & 0 \\ 0 & r_a \end{bmatrix}, r_a > 0. \tag{17}$$

Substituting (16) into the error function of (13), then the error EL model is defined as follows:

$$\begin{aligned} \boldsymbol{M}\dot{\boldsymbol{x_e}} + \boldsymbol{R_d x_e} = & -\boldsymbol{u} + \boldsymbol{M}\dot{\boldsymbol{x}}_{\mathrm{ref}} + \boldsymbol{J}\left(x_{\mathrm{ref}} - \boldsymbol{x_e}\right) \\ & + \boldsymbol{R}\boldsymbol{x}_{\mathrm{ref}} + \boldsymbol{R_a x_e}. \end{aligned} \tag{18}$$

Therefore, the PBC can be designed as

$$\boldsymbol{u} = \boldsymbol{M}\dot{\boldsymbol{x}}_{\mathrm{ref}} + \boldsymbol{J}\boldsymbol{x} + \boldsymbol{R}\boldsymbol{x}_{\mathrm{ref}} + \boldsymbol{R_a x_e}. \tag{19}$$

When the power tracking is accurate enough, the error x_e can fluctuate around zero. The system rapidly converges to the desired equilibrium point and achieves the global stability, when

$$\dot{\boldsymbol{H}}_{\boldsymbol{e}}(\boldsymbol{x}) = \boldsymbol{x_e^T M}\dot{\boldsymbol{x_e}} = -\boldsymbol{x_e^T R_d x_e} = -\boldsymbol{H_e}(\boldsymbol{x})/t_{cr} < 0 \tag{20}$$

where $t_{cr} = L_g/(2R_g + 3r_a)$ means the time constant of convergence. Because of $\boldsymbol{R_a} >> \boldsymbol{R}$, the convergence speed of $\boldsymbol{H_e(x)}$ mainly depends on the $\boldsymbol{R_a}$, which principally determines the robustness of the 3LT^{2}C to system parameter changes and external disturbances [29]. Substituting (14) into (19)

$$\begin{aligned} e_\alpha u_\alpha + e_\beta u_\beta &= E_P \\ &= -\frac{2}{3}L_g\dot{P}_{\text{gref}} - \frac{2}{3}\omega_f L_g Q_g^{\text{ext}} - \frac{2}{3}R_g P_{\text{gref}} \\ &\quad - r_a\left(P_{\text{gref}} - P_g\right) + e_\alpha^2 + e_\beta^2 \\ e'_\alpha u_\alpha + e'_\beta u_\beta &= E_Q \\ &= -\frac{2}{3}L_g\dot{Q}_{\text{gref}}^{\text{ext}} + \frac{2}{3}\omega_f L_g P_g - \frac{2}{3}R_g Q_{\text{gref}}^{\text{ext}} \\ &\quad - r_a\left(Q_{\text{gref}}^{\text{ext}} - Q_g^{\text{ext}}\right) + e'_\alpha e_\alpha + e'_\beta e_\beta. \end{aligned} \tag{21}$$

To simplify the dynamics in (21), we define E_P and E_Q as the new control inputs. Therefore, the original control inputs u_α and u_β can be calculated by (21)

$$\begin{cases} u_\alpha = \frac{e'_\beta E_P - e_\beta E_Q}{e_\alpha e'_\beta - e_\beta e'_\alpha} \\ u_\beta = \frac{e_\alpha E_Q - e'_\alpha E_P}{e_\alpha e'_\beta - e_\beta e'_\alpha}. \end{cases} \tag{22}$$

The abovementioned control method is applied to the nondistorted grid voltage. When unbalanced and distorted grid voltage coexist, the grid currents will be distorted again. Consequently, if we only consider a fundamental frequency of the voltages $e_{f\alpha}$ and $e_{f\beta}$ at PCC, then the grid currents will reduce the content of low-order harmonics (fifth, seventh,...). The fundamental voltages and those quadrature components are extracted by the second-order generalized integral-quadrature signal generator (SOGI-QSG) [32]. The transfer function of SOGI-QSG is as follows:

$$\begin{aligned} G_I(s) &= \frac{e_{f\alpha\beta}(s)}{e_{\alpha\beta}(s)} = \frac{k_s\omega_g s}{s^2 + k_s\omega_g s + \omega_g^2} \\ G_{qI}(s) &= \frac{e'_{f\alpha\beta}(s)}{e_{\alpha\beta}} = \frac{k_s\omega_g^2}{s^2 + k_s\omega_g s + \omega_g^2} \end{aligned} \tag{23}$$

where $\omega_g = \omega_f = 100$ pi rad/s is considered, and k_s is the damping ratio. The signal $e'_{f\alpha\beta}$ is 90° phase-shifted of input signal $e_{f\alpha\beta}$. Thus, the final control law $u_{f\alpha}$ and $u_{f\beta}$ with fundamental voltage injection (FVI) can be derived from (21) and (22).

$$\begin{aligned} e_{f\alpha}u_\alpha + e_{f\beta}u_\beta &= E_{Pf} \\ &= -\frac{2}{3}L_g\dot{P}_{\text{gref}} - \frac{2}{3}\omega_f L_g Q_{fg}^{\text{ext}} - \frac{2}{3}R_g P_{\text{gref}} \\ &\quad - r_a\left(P_{\text{gref}} - P_{fg}\right) + e_{f\alpha}^2 + e_{f\beta}^2 \\ e'_{f\alpha}u_\alpha + e'_{f\beta}u_\beta &= E_{Qf} \\ &= -\frac{2}{3}L_g\dot{Q}_{\text{gref}}^{\text{ext}} + \frac{2}{3}\omega_f L_g P_{fg} - \frac{2}{3}R_g Q_{\text{gref}}^{\text{ext}} \\ &\quad - r_a\left(Q_{\text{gref}}^{\text{ext}} - Q_{fg}^{\text{ext}}\right) + e'_{f\alpha}e_{f\alpha} + e'_{f\beta}e_{f\beta} \end{aligned} \tag{24}$$

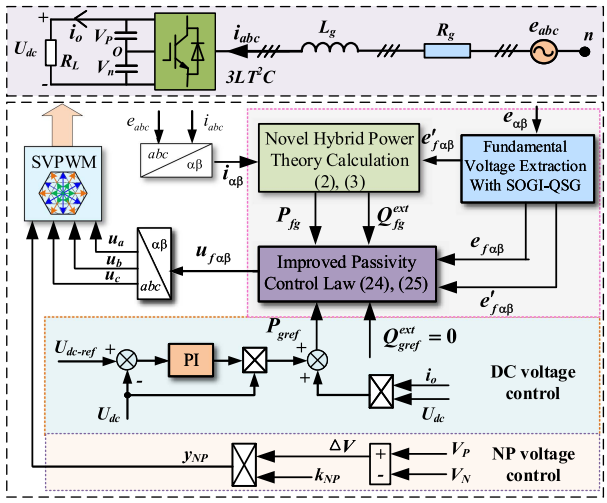

Fig. 2. Control block diagram of the proposed IPBDPC strategy.

$$\begin{cases} u_{f\alpha} = \frac{e'_{f\beta}E_{Pf} - e_{f\beta}E_{Qf}}{e_{f\alpha}e'_{f\beta} - e_{f\beta}e'_{f\alpha}} \\ u_{f\beta} = \frac{e_{f\alpha}E_{Qf} - e_{f\beta}E_{Pf}}{e_{f\alpha}e'_{f\beta} - e_{f\beta}e'_{f\alpha}} \end{cases} \tag{25}$$

where E_{Pf} and E_{Qf} are the fundamental components of E_P and E_Q, $P_{fg} = 1.5Re(i^*_{\alpha\beta}e_{f\alpha f\beta})$, and $Q_{fg}^{\text{ext}} = 1.5Re(i^*_{\alpha\beta}e'_{\alpha\beta})$. The control diagram is shown in Fig. 2. More notably, the proposed IPBDPC method is a compound control that contains a feedback term, a grid voltage feedforward term, and a model-based inverse feedforward term. The feedback term is a damping control. The voltage feedforward term can improve the system's response speed and stability to changes in the grid voltage, whereas the model-based inverse input is used as a feedforward to enhance the output tracking performance. Thus, the 3LT ^{2} C system will have a better steady state and dynamic performance under the proposed method.

C. DC Voltage Loop Design

In order to improve the control ability of dc voltage and robustness, a PI-based dc voltage outer loop control is designed, which is presented as

$$P_{\text{gref}} = \left(k_p + \frac{k_i}{s}\right)\left(U_{\text{dcref}} - U_{\text{dc}}\right) + U_{\text{dc}}i_o \tag{26}$$

where k_p and k_i are the proportional and integral gains of dc voltage control loop, respectively. i_o is the output current of dc side. Therefore, the hybrid control method proposed in this article consists of a dual loop structure, a PI-based dc voltage outer loop, and an IPBDPC inner loop, as shown in Fig. 2.

For neutral-point (NP) balance of 3LT^{2}C, the NP voltage can be controlled by a conventional NP balance control method, which can be achieved by injecting appropriate zero-sequence components into modulated waves u_{abc}. The method of proportional adjustment is designed for controlling the NP voltage in this article, and the injected zero-sequence component is

$$y_{\text{np}} = \pm k_{\text{NP}}\Delta V, k_{\text{NP}} > 0. \tag{27}$$

where k_{NP} is the NP control coefficient, and ΔV is the voltage difference between the upper and lower capacitors.

III. Robustness Analysis Based on Sequence Impedance

In this section, to analyze the grid-connected stability and robustness of the 3LT^{2}C, the sequence impedance model of the IPBDPC is developed. Because the proposed IPBDPC is a direct power control method and the controller is designed based on the $\alpha\beta$ frame, the fixed dc operating point of voltage and current is absent. Therefore, a linearization method based on harmonic interference is designed to linearize the nonlinear terms in the model [34]. The proposed model indicates the closed-loop relation between e_g and i_g. Then, the stability criteria of impedance model under parameter perturbations and external disturbances are carried out to analyze the robustness of the proposed control system. To establish the impedance model, the deduction is carried out from (24) and (25).

$$\begin{cases} u_{f\alpha} = \frac{2}{3}L_g(A_\alpha + B_\alpha) + \frac{2}{3}R_gC_\alpha + r_aD_\alpha + e_\alpha \\ u_{f\beta} = \frac{2}{3}L_g(A_\beta + B_\beta) + \frac{2}{3}R_gC_\beta + r_aD_\beta + e_\beta \end{cases} \tag{28}$$

where $A_\alpha, A_\beta, B_\alpha, B_\beta, C_\alpha$, and C_β are four different coupling terms, D_α and D_β are the coupling terms of injection damping, which can be written as

$$\begin{aligned} A_\alpha &= \frac{-\omega_f Q_{fg}^{\text{ext}} e_{f\alpha} + \omega_f P_{fg} e_{f\beta}}{U_{fg}^2}, A_\beta = \frac{-\omega_f P_{fg} e_{f\alpha} - \omega_f Q_{fg}^{\text{ext}} e_{f\beta}}{U_{fg}^2} \\ B_\alpha &= \frac{-\dot{P}_{\text{ref}} e_{f\alpha} - \dot{Q}_{\text{ref}}^{\text{ext}} e_{f\beta}}{U_{fg}^2}, \quad B_\beta = \frac{-\dot{P}_{\text{ref}} e_{f\beta} + \dot{Q}_{\text{ref}}^{\text{ext}} e_{f\alpha}}{U_{fg}^2} \\ C_\alpha &= \frac{-P_{\text{ref}} e_{f\alpha} - Q_{\text{ref}}^{\text{ext}} e_{f\beta}}{U_{fg}^2}, C_\beta = \frac{-P_{\text{ref}} e_{f\beta} + Q_{\text{ref}}^{\text{ext}} e_{f\alpha}}{U_{fg}^2} \end{aligned} \tag{29}$$

$$\begin{aligned} D_\alpha &= -\frac{e_{f\alpha}}{U_{fg}^2}(P_{\text{ref}} - P_{fg}) - \frac{e_{f\beta}}{U_{fg}^2}(Q_{\text{ref}} - Q_{fg}^{\text{ext}}) \\ D_\beta &= -\frac{e_{f\beta}}{U_{fg}^2}(P_{\text{ref}} - P_{fg}) + \frac{e_{f\alpha}}{U_{fg}^2}(Q_{\text{ref}} - Q_{fg}^{\text{ext}} \end{aligned} \tag{30}$$

where $U_{fg}^2 = e_{f\alpha}^2 + e_{f\beta}^2$.

A. Model Simplification

To further simplify A_α and A_β, substituting (2) and (3) into (28). In addition, P_{ref} and $Q_{\text{ref}}^{\text{ext}}$ are constant under small signal steady-state condition, hence B_α and B_β can be written as follows:

$$\begin{aligned} &A_\alpha = 1.5\omega_f i_\beta, A_\beta = -1.5\omega_f i_\alpha \\ &B_\alpha = 0, \qquad B_\beta = 0. \end{aligned} \tag{31}$$

However, C_α, C_β, D_α, and D_β are non-linear terms, which cannot be directly linearized. The grid voltage $e_{\alpha\beta}$ and current $i_{\alpha\beta}$ after harmonics injection contain fundamental components $e_{f\alpha\beta}$ and $i_{f\alpha\beta}$ and harmonics components $e_{h\alpha\beta}$ and $i_{h\alpha\beta}$, respectively. For D_α and D_β, after the SOGI filtering, the proportion of harmonic component $e_{h\alpha\beta}$ in $e_{\alpha\beta}$ is very small and can be ignored. The U_{fg}^2 in C_α, C_β, D_α, and D_β can be approximated as a dc value. Therefore, the C_α and C_β can be linearized, and the active power and reactive power of P_{fhg} and Q_{fhg}^{ext} after harmonic injection can be approximated as

$$\begin{cases} P_{\text{fhg}} \approx \underbrace{\left(\frac{3}{2}i_{f\alpha\beta} \odot e_{f\alpha\beta}\right)}_{P_{\text{g0}}} + \underbrace{\left(\frac{3}{2}i_{h\alpha\beta} \odot e_{f\alpha\beta}\right)}_{P_{\text{ac}}} \\ Q_{fhg}^{\text{ext}} \approx \underbrace{\left(\frac{3}{2}i_{f\alpha\beta} \otimes v_{f\alpha\beta}\right)}_{Q_{\text{g0}}^{\text{ext}}} + \underbrace{\left(\frac{3}{2}i_{h\alpha\beta} \otimes v_{f\alpha\beta}\right)}_{Q_{\text{ac}}} \end{cases} \tag{32}$$

where $\odot$ and $\otimes$ denote the dot product and cross product of two complex vectors, respectively. P_{g0} and Q_{g0}^{ext} are approximately equal to their reference P_{ref} and Q_{ref} in a steady state, respectively, which has no effect on harmonic frequency domain analysis. By substituting (32) into (30), D_α and D_β can be simplified into

$$\begin{cases} D_\alpha \approx \frac{e_{f\alpha}P_{\text{ac}} + e_{f\beta}Q_{\text{ac}}}{U_{fg}^2} \approx \frac{3}{2}\sum_{\text{h}=1}^{N} i_{h\alpha} \\ D_\beta \approx \frac{e_{f\beta}P_{\text{ac}} - e_{f\alpha}Q_{\text{ac}}}{U_{fg}^2} \approx \frac{3}{2}\sum_{\text{h}=1}^{N} i_{h\beta}. \end{cases} \tag{33}$$

B. Sequence Impedance Modeling

Substituting (31) and (33) into (28), the harmonic reference voltage vectors $u_{h\alpha\beta}$ can be converted to the frequency domain by Laplace transform as follows:

$$\begin{bmatrix} u_{h\alpha} \\ u_{h\beta} \end{bmatrix} = \underbrace{\begin{bmatrix} \frac{3}{2}r_a & L_g\omega_f \\ -L_g\omega_f & \frac{3}{2}r_a \end{bmatrix}}_{Z_{\text{PB}}} \begin{bmatrix} i_{h\alpha} \\ i_{h\beta} \end{bmatrix} + \underbrace{\begin{bmatrix} -\frac{2R_gP_{\text{ref}}G_I(s)}{3U_{fg}^2} + G_I(s) & -\frac{2RQ_{\text{ref}}G_I(s)}{3U_{fg}^2} \\ \frac{2R_gQ_{\text{ref}}G_I(s)}{3U_{fg}^2} & -\frac{2RP_{\text{ref}}G_I(s)}{3U_{fg}^2} + G_I(s) \end{bmatrix}}_{T_{cv}} \begin{bmatrix} e_{h\alpha} \\ e_{h\beta} \end{bmatrix} \tag{34}$$

where Z_{PB} and T_{cv} are the transfer matrix of i_h and e_h to u_h, respectively. The harmonic impedance of the 3LT^{2}C is expressed by Laplace transform from (1) as follows:

$$\begin{bmatrix} e_{h\alpha} \\ e_{h\beta} \end{bmatrix} = \underbrace{\begin{bmatrix} R_g + sL_g & 0 \\ 0 & R_g + sL_g \end{bmatrix}}_{\boldsymbol{Z}_{LR}} \begin{bmatrix} i_{h\alpha} \\ i_{h\beta} \end{bmatrix} + \begin{bmatrix} u_{h\alpha} \\ u_{h\beta} \end{bmatrix}. \tag{35}$$

Substituting (34) into (35), the impedance model considering harmonic components can be calculated as

$$\begin{aligned} \begin{bmatrix} e_{h\alpha} \\ e_{h\beta} \end{bmatrix} &= (\boldsymbol{I} - \boldsymbol{T}_{cv})^{-1}(Z_{LR} + Z_{PB}) \begin{bmatrix} i_{h\alpha} \\ i_{h\beta} \end{bmatrix} \\ &= \underbrace{\begin{bmatrix} Z_{\alpha\alpha}(s) & Z_{\alpha\beta}(s) \\ Z_{\beta\alpha}(s) & Z_{\beta\beta}(s) \end{bmatrix}}_{\boldsymbol{Z}_{T^2C}} \begin{bmatrix} i_{h\alpha} \\ i_{h\beta} \end{bmatrix} \end{aligned} \tag{36}$$

where the Z_{T^2C} represents the final impedance matrix. The equivalent sequence-impedance transfer function can be expressed as [34]

$$\begin{cases} Z_{\text{T}^2\text{C,p}}(s) = \frac{Z_{\alpha\alpha}(s) + Z_{\beta\beta}(s)}{2} + j\frac{Z_{\beta\alpha}(s) - Z_{\alpha\beta}(s)}{2} \\ Z_{\text{T}^2\text{C,n}}(s) = \frac{Z_{\alpha\alpha}(s) - Z_{\beta\beta}(s)}{2} + j\frac{Z_{\beta\alpha}(s) + Z_{\alpha\beta}(s)}{2}. \end{cases} \tag{37}$$

Since the diagonal elements of the 2-D impedance matrix have symmetric characteristics, $Z_{\alpha\alpha} = Z_{\beta\beta}$, $Z_{\alpha\beta} = -Z_{\beta\alpha}$, it can

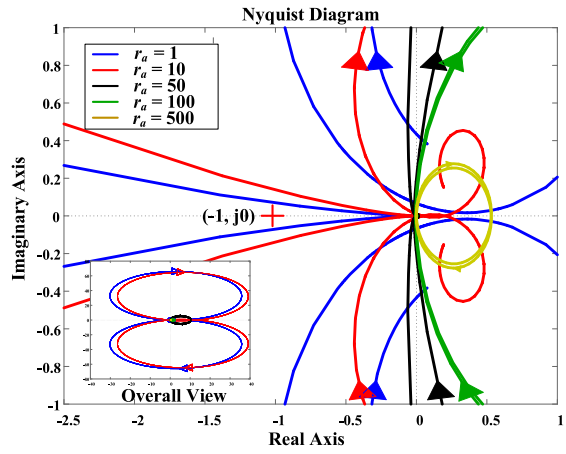

(a)

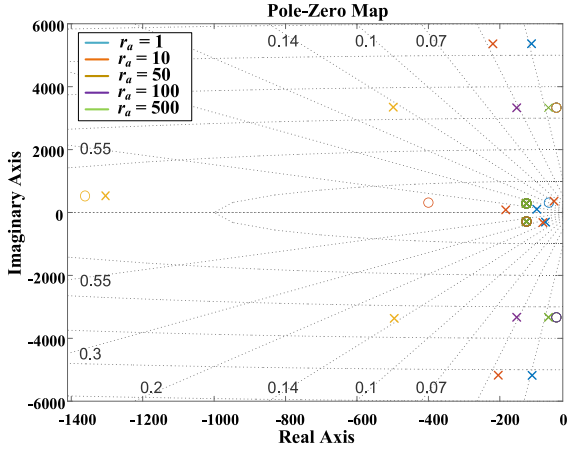

(b)

Fig. 3. Stability analysis with different control parameters r_a. (a) Nyquist diagram of IR_{recp}, (b) Pole-zero map of G_Z.

be inferred that $Z_{\text{T}^2\,\text{C,n}}(s) = 0$. Then, it is assumed that the impedance of the power grid is

$$Z_{\text{grid}}(s) = \frac{L_{\text{n}}s + R_{\text{n}}}{(L_{\text{n}}s + R_{\text{n}})\,C_{\text{n}}s + 1} \tag{38}$$

where the R_n and L_n are grid resistance and inductance, respectively, and C_n is the parallel capacitor. In this case, the stability of the system can be identified by the impedance ratio of $IR_{\text{recp}}(s) = Z_{\text{grid}}(s)/Z_{\text{T}^2\,\text{C,p}}(s)$ and its closed-loop transfer function $G_Z(s) = 1/(1 + IR_{\text{recp}}(s))$ [33].

C. Robustness Analysis

When L and r_a changes, the Nyquist diagrams of $IR_{\text{recp}}(s)$ are shown in Figs. 3 and 4. The parameters of the 3LT^{2}C are listed in Table I.

The characteristic loci will not surround the stable point $(-1,$ j0) under five different control parameters, which proves the passivity and stability of the system, as shown in Fig. 3(a). From the overall view, it can be seen that the larger the damping value, the smaller the intersection value between the Nyquist diagram and the imaginary axis, which means that control degree is increasing. For larger/smaller values of damping ($r_a = 1, 10,...$ 500), the dominant poles are getting closer to the imaginary axis,

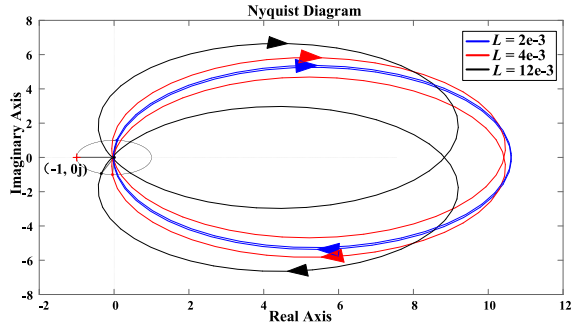

Fig. 4. Nyquist diagram of IR_{recp} with filtering inductance changes.

TABLE I
PARAMETERS FOR SIMULATION AND EXPERIMENT

Parameters	Values
AC grid voltage (RMS)	110 V
DC reference voltage (U_{dcref})	400 V
Switch frequency	10 kHz
Sampling period	100 μs
Rated active power	3000W
Filter inductors(L_g)	4 mH
Filter resistance(R_g)	0.1 Ω
Fundamental frequency(ω_f)	100*pi
DC-link capacitors (C_1, C_2)	1875 μF
DC load	65 Ω
Line resistance / inductance (R_n/L_n)	0.5 Ω / 10 mH
Line capacitance (C_n)	15 μF
Control parameters (r_{a1}, r_{a2})	50
SOGI-QSG resonance coefficient (k_s)	0.707
DC voltage control coefficient (k_p)	0.1
DC voltage control coefficient (k_i)	4
NP control coefficient (k_{NP})	0.07

which may lead to an undesired stability margin, as shown in Fig. 3(b). In addition, Thus, the values of r_a can be manually fine-tuned from small to large until the satisfactory response is achieved within the range of constraint conditions. As shown in Fig. 4, with the change of the filter inductance value, the Nyquist diagram never surrounds $(-1,$ j0) points, which again proves the stability of the system. In general, the proposed IPBDPC method is robust to parameters perturbations of the controller and hardware circuit.

D. Tuning of Parameters

The parameters tuning principle for damping ratio of SOGI-QSG and the injection damping of PBC are given as follows.

The core of SOGI-QSG is a bandpass filter, and the performance of the second-order filter used in (23) is not affected by ω_g, but changes with the damping ratio k_s. The Bode diagram of $G_I(s)$ and $G_{qI}(s)$ is shown in Fig. 5. It can be seen that the smaller the k_s, the better the filtering effect, but the slower the response speed. Considering the filtering effect and response time comprehensively, $k_s = 0.707$ is selected.

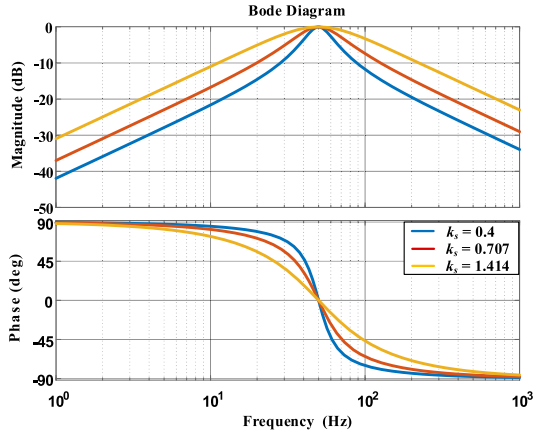

(a)

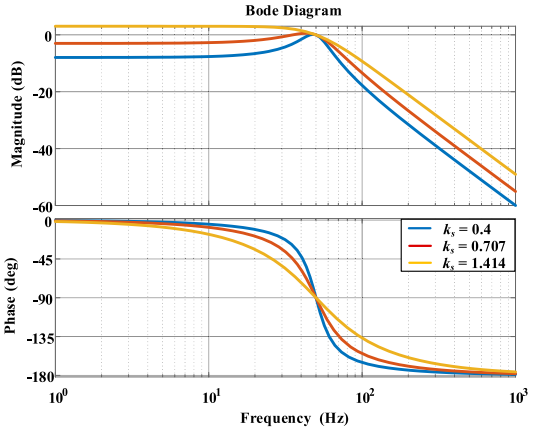

(b)

Fig. 5. Frequency response characteristics of (a) $G_I(s)$ and (b) $G_{qI}(s)$.

For the injection damping r_a, the passivity of the controller must be satisfied first. The error function $H_e > 0$ and $\dot{H}_e < 0$ rely on r_a, if r_a is negative, the strict passive conditions are unable to meet for the converter system.

$$R_g + r_a > 0. \tag{39}$$

Then, according to the cascaded dual loop control structure, the corresponding speed of the power inner loop should be much faster than that of the dc voltage outer loop (more than 10 times). We have

$$t_{\rm dc} \geq 10t_{cr} = 10L_g/(2R_g + 3r_a). \tag{40}$$

From (39), r_a satisfies

$$r_a \geq \frac{10L_g}{t_{\rm dc}} - \frac{2R_g}{3}. \tag{41}$$

However, it should be noted that larger damping can increase the control bandwidth of the controller while diminishing the suppression of high-frequency harmonics in the current, as shown in Fig. 6, which will reduce the robustness against the measurement noise and high-frequency ripple. Thus, the values of damping gain can be adjusted reasonably from small to large until a satisfactory response is obtained.

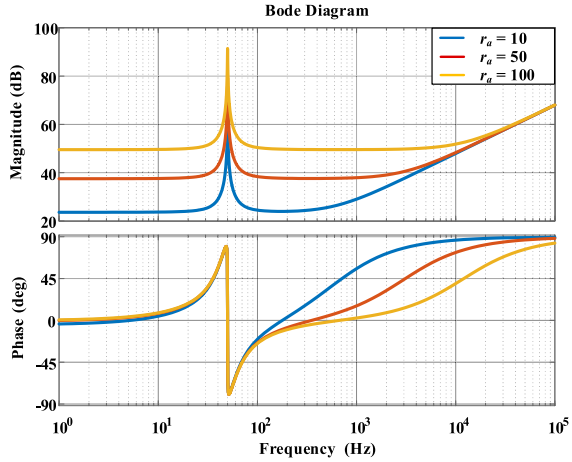

Fig. 6. Bode diagram of sequence impedance $Z_{\rm T^2\,C,p}(s)$ under different injection damping r_a.

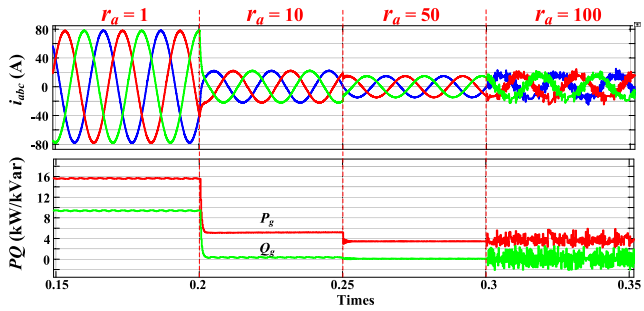

Fig. 7. Performance comparison for 3LT^{2}C with different damping values ($r_a = 1, 10, 50, 100$).

IV. Simulation and Experimental Results

A. Simulation Results

In this section, a 3LT^{2}C system, based on the system schematic diagram shown in Fig. 1, is built in MATLAB/Simulink to verify the effectiveness of the proposed IPBDPC method. The control and system parameters are given in Table I. A resistive load is connected to the dc-side for performance testing. The comparison with DPC-PIR [16] and VOC-DSRF [8] is carried out to fully analyze the performance of the IPBDPC method.

To investigate the effect of the 3LT^{2}C parameters' uncertainties on the control performance, the simulations with deviation sets of the real control parameter r_a and the inductance L have been run, as shown in Figs. 7 and 8. When the damping value r_a changes from 1 to 100, the output power is always stable, as shown in Fig. 7. However, if the control damping value r_a is too low, the control force will be insufficient, resulting in a sizeable steady-state error. Beyond that, if the control damping value $r_a = 100$, excessive control will lead to high-frequency harmonics in grid current. When the filter inductances are switched from $0.5L$ to L and then to $3L$, the current and power of 3LT^{2}C can be continuously stable under the proposed IPBDPC compared with VOC-DSRF and DPC-PIR methods, as shown in Fig. 8.

When the voltage of phase A drops by 50%, and three-phase grid voltage contain 5% fifth harmonic and 5% seventh

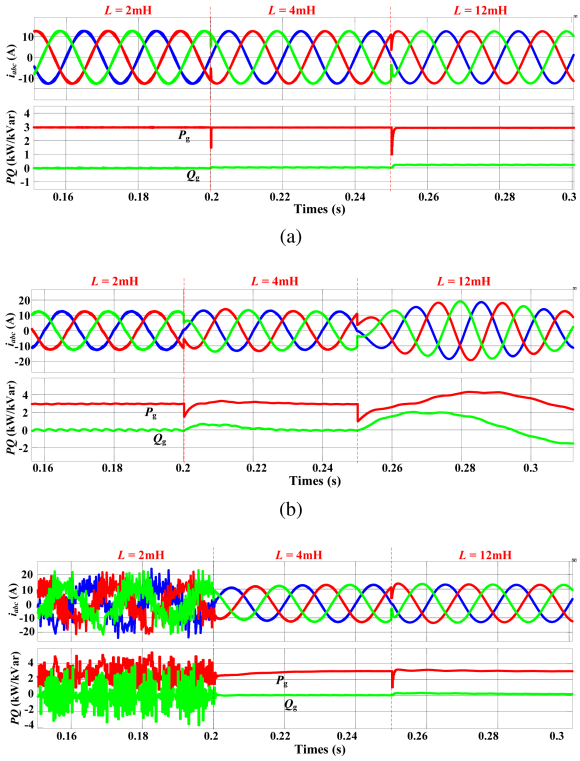

Fig. 8. Performance comparison of 3LT^{2}C with different Filter inductance value ($L = 2, 4, 12$ mH). (a) Proposed IPBDPC. (b) VOC-DSRF. (c) DPC-PIR.

TABLE II
COMPARISON OF FOUR CONTROL METHODS UNDER UNBALANCED AND DISTORTED GRID REGARDING HARMONIC CONTENTS OF CURRENT

Harmonic Frequency	3th	5th	7th
ERPT-based DPC-PIR	10.60%	3.14%	6.41%
PBDPC	16.97%	2.83%	0.82%
Proposed IPBDPC without FVI	6.60%	1.23%	6.17%
Proposed IPBDPC with FVI	1.09%	1.25%	0.42%

harmonic, the comparative results under the ERPT-based DPC-PIR method [17], traditional PBDPC, proposed IPBDPC without FVI, and proposed IPBDPC with FVI are shown in Fig. 9. For the more reasonable performance comparisons, the outer loops of the abovementioned four control methods are all PI-based dc voltage loops with same control parameters. The harmonic contents of grid currents under different control methods are given in Table II. It can be seen that the ERPT-based DPC-PIR method strategy can suppress the active power oscillation, and the amplitude of active power oscillation reaches 700 W. But the grid current distortion is severe, and the third harmonic content even goes 10.60%, indicating that the negative sequence grid voltage has a significant impact. The amplitude of active power oscillation is 900 W under IPT-based PBDPC strategy. In addition, the grid currents contain more fifth and seventh harmonics, which indicate that it is greatly affected by grid voltage harmonics and imbalance. For the proposed IPBDPC without FVI, the distortion of the currents has been improved, but the currents still contain third and seventh harmonics due to the influence of grid harmonics. For the proposed IPBDPC with FVI, the active power oscillation has been further suppressed, with an amplitude of only 270 W. In addition, the harmonics in the grid-side current are greatly suppressed, and the harmonic contents of the third, fifth, and seventh are less than 1.25%, respectively. In general, the proposed IPBDPC strategy is robust against parameter perturbations and external disturbances, and can achieve the active power oscillation and current harmonics suppression when the grid voltage imbalance and distortion coexist.

B. Experimental Results

The experiment is conducted based on a prototype of a three-phase 3LT^{2}C to verify the feasibility of the proposed IPBDPC strategy, as shown in Fig. 10. The experimental system contains a programmable ac source, a digital controller (based on dSPACE DS1007 and CPLD), main power system with driver circuits, IGBT T-type modulars, L-filters, and dc resistive load. The system parameters are given in Table I. Fig. 11 shows comparative results for the ERPT-based DPC-PIR, PBDPC, and proposed IPBDPC when A phase voltage drops by 50%. It is seen that the amplitude of active power oscillation is suppressed to 600 W, the dc voltage ripple is 3.5 V, and the THD of the current is reduced to 3.89% by ERPT-based DPC-PIR method, as shown in Fig. 11(a). Then, compared with the traditional PBDPC method, the proposed IPBDPC method effectively suppresses active power oscillation and current harmonics, as shown in Fig. 11(b) and (c). The amplitude of active power oscillation and dc voltage ripple are only 250 W and 2.5 V, respectively, and the THD of the currents is 1.49%. It can be seen that the proposed IPBDPC method has significant advantages in suppressing grid current distortion and dc voltage ripple under unbalanced grid voltage conditions, as shown in Fig. 12. Compared with traditional PBDPC, the THD of currents has a 70% improvement, and the dc voltage ripple is 48% smaller. Compared with the ERPT-based DPC-PIR, due to the advantages of nonlinearity and robustness of the proposed IPDPC, the dc voltage ripple suppression and current harmonics reduction of the 3LT^{2}C have been further improved. Specifically, the THD of the currents has been reduced by 62%. Therefore, the proposed method is more suitable for ac/dc power conversion at the power grid port of the PR, which can stably operate under unbalanced grid voltage conditions without increasing the capacity of ac-side filters and dc-side capacitors.

To verify the harmonic suppression ability of the proposed IPBDPC method, 3% of the fifth harmonic and 5% of the seventh harmonic are injected into the grid voltage. As shown in Fig. 13, the proposed method can not entirely suppress current harmonics without FVI, and the THD is 5.46%. However, the injection of fundamental voltages strengthens the harmonic suppression ability of IPBDPC, and the THD is reduced to 2.13%. This indicates that the injection of fundamental voltages can significantly increase the robustness of the system and greatly improve the range of operating conditions to the 3LT^{2}C. Even the THD of the currents can be further reduced by 61%. When A phase voltage drops by 50% and three-phase voltages are injected with 3% fifth harmonic and 5% seventh harmonic, steady-state responses for the ERPT-based DPC-PIR, PBDPC, and proposed IPBDPC

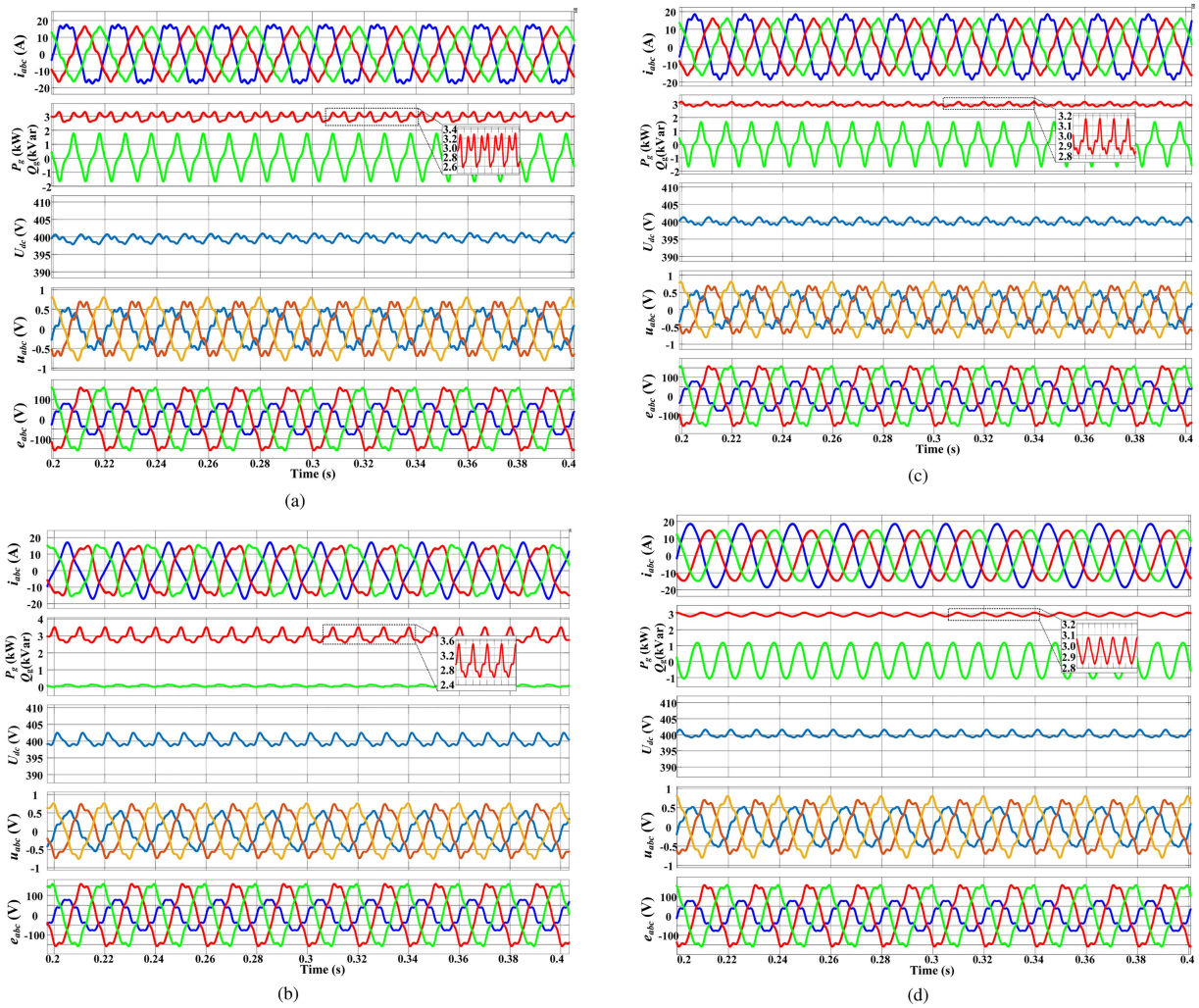

Fig. 9. Steady-state performances of i_{abc}, P_g, Q_g, $u_{\rm dc}$, and u_{abc}, under unbalanced and distorted grid voltage for (a) ERPT-based DPC-PIR, (b) PBDPC, (c) proposed IPBDPC without FVI, and (d) proposed IPBDPC with FVI.

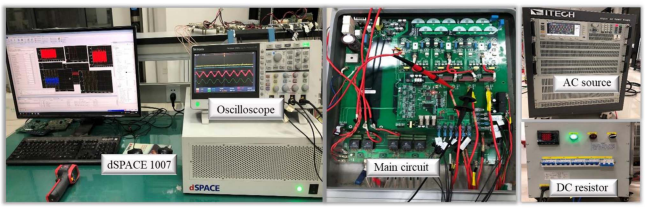

Fig. 10. Experimental photograph of the 3LT^{2}C system.

are shown in Fig. 14. The grid currents are seriously distorted in ERPT-based DPC-PIR and PBDPC, whose THDs reach 6.21% and 5.75%, respectively. For the IPBDPC, although THD of grid currents are 2.09%, it is still within the grid connection requirements specified by IEEE. In contrast, the dc voltage ripple is only 3 V under the proposed method, indicating that the active power oscillation has still been effectively suppressed, as shown in Fig. 15. In general, the proposed IPBDPC can not only adapt to unbalanced and balanced grid voltage, but also maintain good steady-state performance when grid voltages are slightly distorted.

Under ideal grid voltage, when the command value of the $U_{\rm dc}$ changes from 350 to 400 V, the active power can be quickly switched, and the current quickly changes from 10 to 14 A, as shown in Fig. 16(a). When the the $Q_{\rm gref}^{\rm ext}$ is increased from 0 to 1 kvar, the active reactive power can be switched quickly without any influence on current and active power, as shown in Fig. 16(b). When the grid voltage is unbalanced and distorted, dc-side voltage and grid current can be switched smoothly, which proves that the proposed IPBDPC achieves good dynamic performance under extreme conditions, as shown in Fig. 17. In addition, the $Q_{\rm gref}^{\rm ext}$ can be quickly switched between 0 and 1000 Var, and the $U_{\rm dc}$ does not fluctuate. The rapid injection of reactive current has no effect on the stability of the system, as shown in Fig. 18. Compared with ideal grid voltage condition, although there are some power oscillations, the dynamic response speed of power converter is not affected, and the system can operate stably.

In summary, under the unbalanced and distorted power grid, the proposed IPBDPC method realizes the sine of grid-connected current and avoids the secondary pollution of grid voltage. The active power oscillation is substantially suppressed,

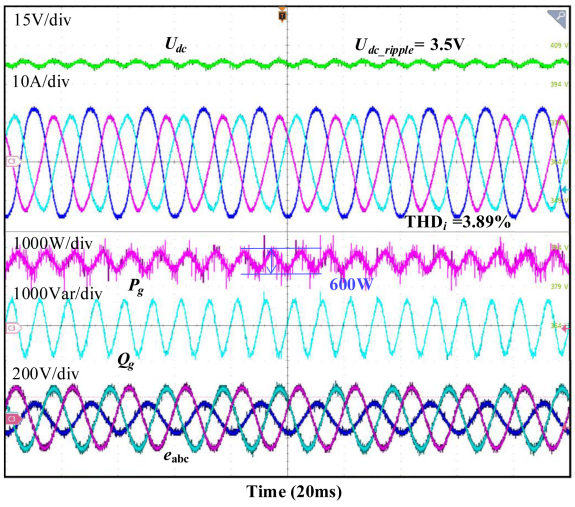

(a)

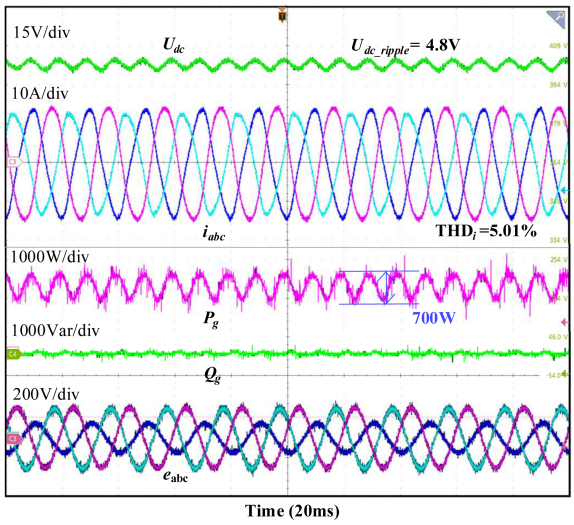

(b)

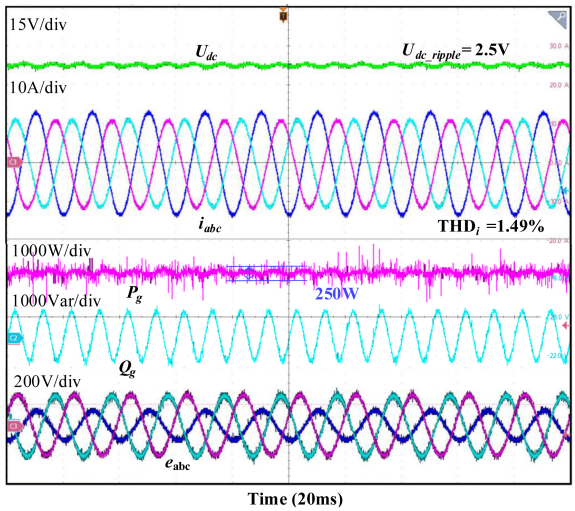

(c)

Fig. 11. Steady-state performances of $U_{\rm dc}$, i_{abc}, active power and reactive power under unbalanced grid voltage for (a) ERPT-based DPC-PIR, (b) PBDPC, and (c) proposed IPBDPC.

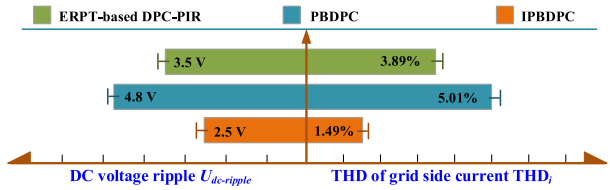

Fig. 12. Comparison of THD$_i$ and DC voltage ripple for ERPT-based DPC-PIR, PBDPC, and proposed IPBDPC methods under unbalanced grid voltage conditions.

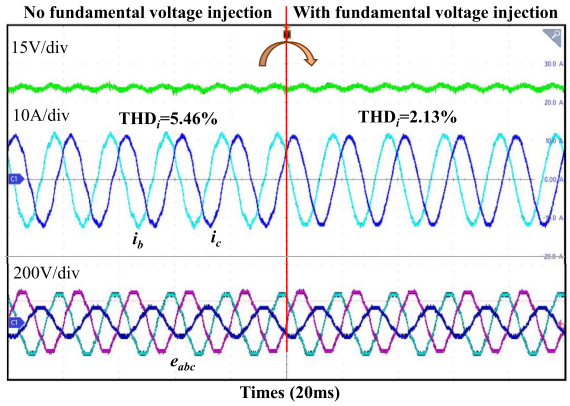

Fig. 13. Steady-state performances of $U_{\rm dc}$ and i_{ab} for the proposed IPBDPC method under FVI and no FVI.

and the dc-side voltage can always maintain a low ripple, which will not affect other ports of the PR. In addition, under extreme working conditions, the dynamic response speed is not affected, which verifies the robustness of the proposed IPBDPC.

V. Conclusion

In this article, an IPBDPC method for 3LT^{2}C suitable for an unbalanced and distorted grid was proposed. The main conclusions could be summarized as follows.

1) The theoretical analysis of the DPC method indicates that traditional PBDPC is not suitable for nonideal grid conditions, such as unbalanced and distorted grid voltages, which could lead to current distortion and dc voltage ripple of the 3LT^{2}C.
2) An improved IPBDPC model was rebuilt by introducing the extended reactive power theory, the fundamental-frequency grid voltages and their quadrature components. Therefore, the improved control strategy can reduce the THD of the grid current and suppress dc voltage ripple when unbalanced and distorted grid conditions coexist.
3) The sequence impedance model of the 3LT^{2}C was constructed based on the proposed IPBDPC method in $\alpha\beta$ frame. Detailed design procedures, robustness and stability analysis, and parameters tuning methods were investigated, indicating that appropriate parameters design could make the converter highly robust to parameter uncertainties and disturbances.
4) Compared with the DPC-PIR and VOC-DSRF methods, the proposed IPBDPC method did not need complex positive and negative sequence separations and power

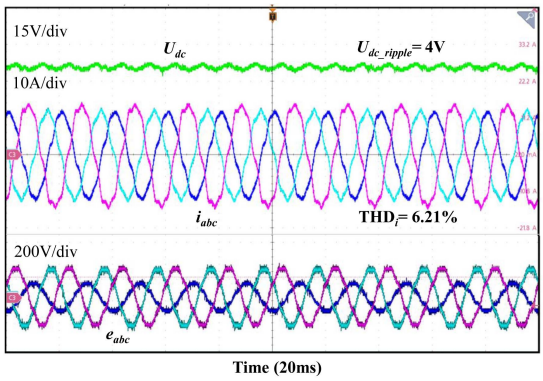

(a)

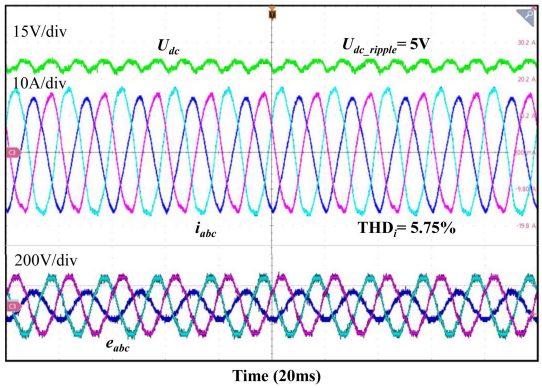

(b)

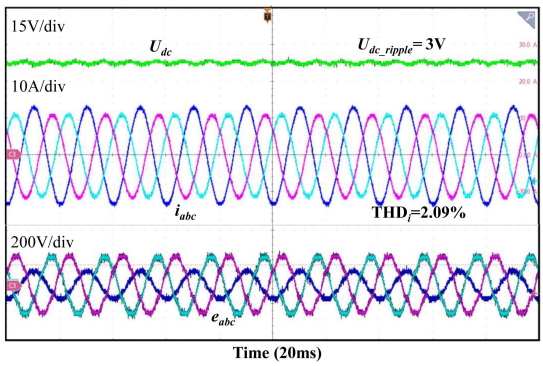

(c)

Fig. 14. Steady-state performances of $U_{\rm dc}$, i_{abc}, active power and reactive power under unbalanced and distorted grid voltages for (a) ERPT-based DPC-PIR, (b) PBDPC, and (d) proposed IPBDPC with FVI.

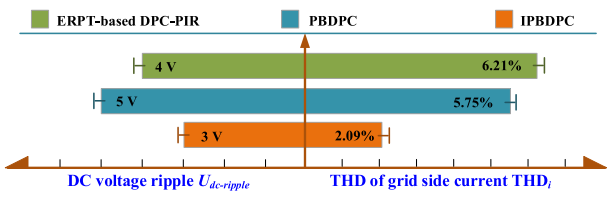

Fig. 15. Comparison of THD$_i$ and DC voltage ripple for ERPT-based DPC-PIR, PBDPC, and proposed IPBDPC methods under unbalanced and distorted grid voltage conditions.

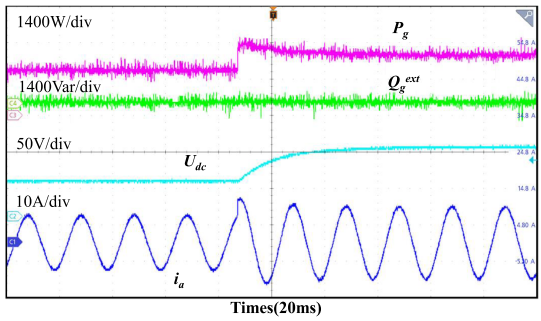

(a)

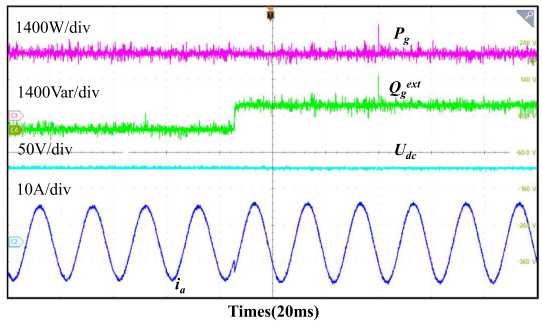

(b)

Fig. 16. Dynamic response of active and reactive power, $U_{\rm dc}$, and phase current under ideal grid voltage. (a) $U_{\rm dc}$ variation of $U_{\rm dcref} = 350 \rightarrow 400$ V. (b) Reactive power variation of $Q_{gref} = 0 \rightarrow 1$ kVar.

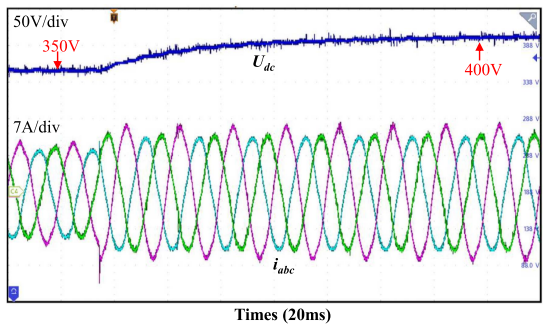

(a)

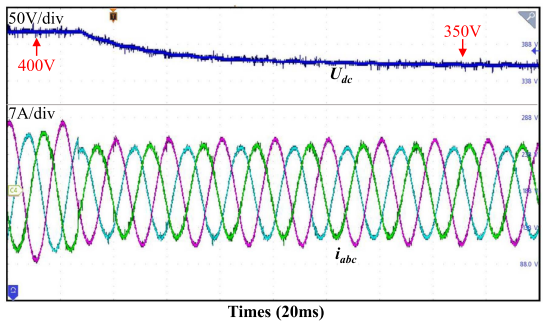

(b)

Fig. 17. Dynamic responses when $U_{\rm dcref}$ steps from 350 to 400 V under unbalanced and distorted grid voltage for the proposed IPBDPC method.

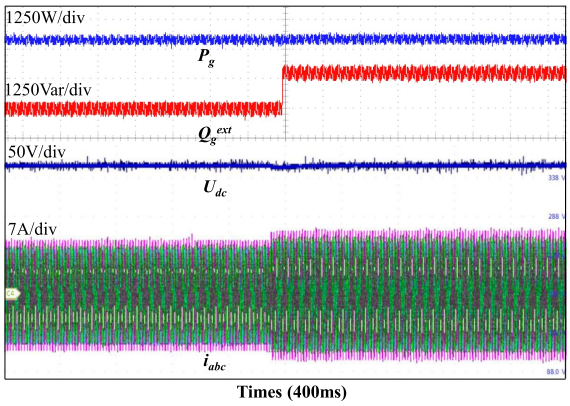

(a)

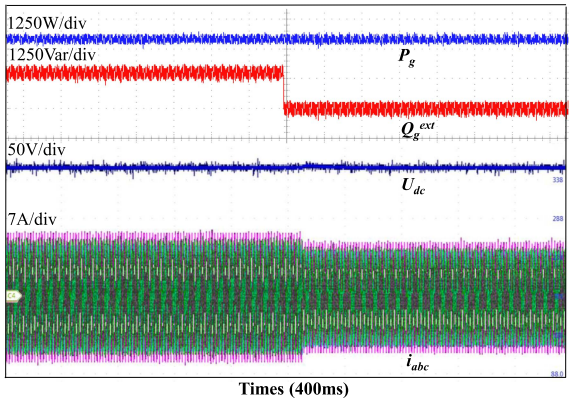

(b)

Fig. 18. Dynamic responses when Q_g^{ext} steps from 0 to 1000 Var under unbalanced and distorted grid voltage for the Proposed IPBDPC method.

reference value calculations, and had strong robustness with a simple control structure. The experimental results indicated that the THD of grid-side current was reduced by 62% compared with the ERPT-based DPC-PIR method. The voltage ripple of dc side was reduced by 48% compared with the PBDPC method. In terms of active power following and reactive power compensation, the proposed IPBDPC method also had good dynamic performance, which fully met the requirements of PR.

REFERENCES

[1] C. Tu, F. Xiao, Z. Lan, Q. Guo, and Z. Shuai, "Analysis and control of a novel modular-based energy router for DC microgrid cluster," *IEEE Trans. Emerg. Sel. Topics Power Electron.*, vol. 7, no. 1, pp. 331–342, Mar. 2019.

[2] S. Niu, T. Liu, X. Liu, Q. Ren, Z. Chen, and A. Chen, "A virtual inertia control strategy with current feedforward to improve voltage stability for power router," in *Proc. 47th Annu. Conf. IEEE Ind. Electron. Soc.*, 2021, pp. 1–6.

[3] J. Lin, M. Su, W. Xiong, S. Xie, Y. Sun, and Y. Zhang, "Conductance emulating control strategy for three-phase current source rectifier under unbalanced grid voltages," *IEEE Trans. Circuits Syst. II, Exp. Briefs*, vol. 69, no. 6, pp. 2837–2841, Jun. 2022.

[4] M. Shahparasti, M. Mohamadian, P. T. Baboli, and A. Yazdianp, "Toward power quality management in hybrid AC–DC microgrid using LTC-L utility interactive inverter: Load voltage-grid current tradeoff," *IEEE Trans. Smart Grid*, vol. 8, no. 2, pp. 857–867, Mar. 2017.

[5] L. Zheng, H. Geng, and G. Yang, "Fast and robust phase estimation algorithm for heavily distorted grid conditions," *IEEE Trans. Ind. Electron.*, vol. 63, no. 11, pp. 6845–6855, Nov. 2016.

[6] S. Xie, Y. Sun, J. Lin, M. Su, X. Li, and X. Zhang, "Resistance-emulating control strategy for three-phase voltage source rectifiers under unbalanced grids," *IEEE Trans. Ind. Electron.*, vol. 69, no. 2, pp. 1103–1113, Feb. 2022.

[7] N. Jiao et al., "The closed-loop sideband harmonic suppression for CHB inverter with unbalanced operation," *IEEE Trans. Power Electron.*, vol. 37, no. 5, pp. 5333–5341, May 2022.

[8] Y. Suh and T. A. Lipo, "Control scheme in hybrid synchronous stationary frame for PWM AC/DC converter under generalized unbalanced operating conditions," *IEEE Trans. Ind. Appl.*, vol. 42, no. 3, pp. 825–835, May/Jun. 2006.

[9] P. D. Achlerkar and B. K. Panigrahi, "New perspectives on stability of decoupled double synchronous reference frame PLL," *IEEE Trans. Power Electron.*, vol. 37, no. 1, pp. 285–302, Jan. 2022.

[10] G. Wang, X. Wang, and J. Lv, "An improved harmonic suppression control strategy for the hybrid microgrid bidirectional AC/DC converter," *IEEE Access*, vol. 8, pp. 220422–220436, 2020.

[11] H. Ahmed, S. Biricik, and M. Benbouzid, "Extended self-tuning filter-based synchronization technique for unbalanced and distorted grid," in *Proc. 2nd Int. Conf. Smart Power Internet Energy Syst.*, 2020, pp. 350–355.

[12] A. Ranjan, S. Kewat, and B. Singh, "Reweighted L_1 norm penalized LMS fourth algorithm of solar grid interfaced system for alleviating power quality problems," *IEEE Trans. Ind. Appl.*, vol. 56, no. 5, pp. 5352–5362, Sep./Oct. 2020.

[13] I. Etxeberria-Otadui, U. Viscarret, M. Caballero, A. Rufer, and S. Bacha, "New optimized PWM VSC control structures and strategies under unbalanced voltage transients," *IEEE Trans. Ind. Electron.*, vol. 54, no. 5, pp. 2902–2914, Oct. 2007.

[14] Y. Gui, M. Li, J. Lu, S. Golestan, J. M. Guerrero, and J. C. Vasquez, "A voltage modulated DPC approach for three-phase PWM rectifier," *IEEE Trans. Ind. Electron.*, vol. 65, no. 10, pp. 7612–7619, Oct. 2018.

[15] A. Fekik, H. Denoun, N. Benamrouche, N. Benyahia, A. Badji, and M. Zaouia, "Comparative analysis of direct power control and direct power control with space vector modulation of PWM rectifier," in *Proc. 4th Int. Conf. Control Eng. Inf. Technol.*, 2016, pp. 1–6.

[16] J. Ge, Z. Zhao, L. Yuan, T. Lu, and F. He, "Direct power control based on natural switching surface for three-phase PWM rectifiers," *IEEE Trans. Power Electron.*, vol. 30, no. 6, pp. 2918–2922, Jun. 2015.

[17] H. Nian, Y. Shen, H. Yang, and Y. Quan, "Flexible grid connection technique of voltage-source inverter under unbalanced grid conditions based on direct power control," *IEEE Trans. Ind. Appl.*, vol. 51, no. 5, pp. 4041–4050, Sep./Oct. 2015.

[18] N. Jin, S. Hu, C. Gan, and Z. Ling, "Finite states model predictive control for fault-tolerant operation of a three-phase bidirectional AC/DC converter under unbalanced grid voltages," *IEEE Trans. Ind. Electron.*, vol. 65, no. 1, pp. 819–829, Jan. 2018.

[19] Y. Gui, Q. Xu, F. Blaabjerg, and H. Gong, "Sliding mode control with grid voltage modulated DPC for voltage source inverters under distorted grid voltage," *CPSS Trans. Power Electron. Appl.*, vol. 4, no. 3, pp. 244–254, Sep.. 2019.

[20] Y. Zhang, J. Jiao, J. Liu, and J. Gao, "Direct power control of PWM rectifier with feedforward compensation of DC-Bus voltage ripple under unbalanced grid conditions," *IEEE Trans. Ind. Appl.*, vol. 55, no. 3, pp. 2890–2901, May/Jun. 2019.

[21] X. Ran, B. Xu, K. Liu, and J. Zhang, "An improved low-complexity model predictive direct power control with reduced power ripples under unbalanced grid conditions," *IEEE Trans. Power Electron.*, vol. 37, no. 5, pp. 5224–5234, May 2022.

[22] D. Zhou, P. Tu, and Y. Tang, "Multivector model predictive power control of three-phase rectifiers with reduced power ripples under nonideal grid conditions," *IEEE Trans. Ind. Electron.*, vol. 65, no. 9, pp. 6850–6859, Sep. 2018.

[23] X. Mu, J. Wang, W. Wu, and F. Blaabjerg, "A modified multifrequency passivity-based control for shunt active power filter with model-parameter-adaptive capability," *IEEE Trans. Ind. Electron.*, vol. 65, no. 1, pp. 760–769, Jan. 2018.

[24] J. Wang, X. Mu, and Q.-K. Li, "Study of passivity-based decoupling control of T-NPC PV grid-connected inverter," *IEEE Trans. Ind. Electron.*, vol. 64, no. 9, pp. 7542–7551, Sep. 2017.

[25] J. Li, M. Wang, Y. Zhao, J. Wang, D. Yang, and X. Lv, "Passivity-based control of the hybrid rectifier for medium and high-power application," *IET Power Electron.*, vol 12, no. 15, pp. 4070–4078, 2019.

[26] T.-S. Lee, "Lagrangian modeling and passivity-based control of three-phase AC/DC voltage-source converters," *IEEE Trans. Ind. Electron.*, vol. 51, no. 4, pp. 892–902, Aug. 2004.

[27] Y. Jiang, J. Wang, Q. Li, Y. Feng, and X. Mu, "The passivity-based hybrid control of NPC hybrid three phase voltage source rectifier," in *Proc. IEEE Int. Power Electron. Application Conf. Expo.*, 2018, pp. 1–6.
[28] Y. Lei, X. Lin, and Y. Zhu, "Passivity-based control strategy for SMES under an unbalanced voltage condition," *IEEE Access*, vol. 6, pp. 28768–28776, 2018.
[29] Y. Jiang, C. Qin, X. Xing, X. Li, and C. Zhang, "A hybrid passivity-based control strategy for three-level T-type inverter in LVRT operation," *IEEE Trans. Emerg. Sel. Topics Power Electron.*, vol. 8, no. 4, pp. 4009–4024, Dec. 2020.
[30] J. Li et al., "Passivity-based control with active disturbance rejection control of vienna rectifier under unbalanced grid conditions," *IEEE Access*, vol. 8, pp. 76082–76092, 2020.
[31] M. Schweizer and J. W. Kolar, "Design and implementation of a highly efficient three-level T-type converter for low-voltage applications," *IEEE Trans. Power Electron.*, vol. 28, no. 2, pp. 899–907, Feb. 2013.
[32] S. Wang, Z. Yuan, J. Ma, T. Liu, Z. Wu, and R. Wang, "Accurate LTP model and stability analysis of the second-order generalized integrator-based single-phase phase-locked loop," *IEEE Trans. Ind. Electron.*, vol. 69, no. 6, pp. 6225–6235, Jun. 2022.
[33] S. Gao, H. Zhao, Y. Gui, J. Luo, and F. Blaabjerg, "Impedance analysis of voltage source converter using direct power control," *IEEE Trans. Energy Convers.*, vol. 36, no. 2, pp. 831–840, Jun. 2021.
[34] M. Cespedes and J. Sun, "Impedance modeling and analysis of grid-connected voltage-source converters," *IEEE Trans. Power Electron.*, vol. 29, no. 3, pp. 1254–1261, Mar. 2014.

Qicai Ren received the B.S. degree in electrical engineering and automation from the Qilu University of Technology, Jinan, China, in 2017. He is currently working toward the Ph.D. degree in electrical engineering with the School of Control Science and Engineering, Shandong University, Jinan, China.

His current research interests include multilevel inverters, renewable power generation, power quality control, and stability analysis and improvement

Alian Chen (Member, IEEE) received the B.S. degree in applied electronics technology and the M.S. degree in power electronics and power transmission from Shandong University, Jinan, China, in 1998 and 2000, respectively, and the Ph.D. degree in electrical engineering from Zhejiang University, Hangzhou, China, in 2005.

She joined the School of Control Science and Engineering, Shandong University, and was promoted as an Associate Professor in 2005. Since 2010, she has been a Full Professor with Shandong University. During 2013 to 2014, she was a Visiting Scholar with the Center for Power Electronics Systems, Virginia Tech, Blacksburg, VA, USA. Her current research interests include multilevel converters, renewable power generation, and microgrids.

Jingyang Fang (Senior Member, IEEE) received the B.Sc. and M.Sc. degrees in electrical engineering from Xi'an Jiaotong University, Xi'an, China, in 2013 and 2015, respectively, and the Ph.D. degree in electrical and electronic engineering from the School of Electrical and Electronic Engineering, Nanyang Technological University, Singapore, in 2019.

From May 2018 to August 2018, he was a Visiting Scholar with the Institute of Energy Technology, Aalborg University, Aalborg, Denmark. From August 2018 to August 2019, he was a Research Fellow with the School of Electrical and Electronic Engineering, Nanyang Technological University, Singapore. From August 2019 to August 2021, he was a Postdoctoral Researcher with the Duke University, Durham, NC, USA, and TU Kaiserslautern, Kaiserslautern, Germany. Since August 2021, he has been with the School of Control Science and Engineering, Shandong University, Jinan, China, as a Full Professor. His research interests include power quality control, stability analysis and improvement, renewable energy integration, and digital control in more-electronics power systems.

Dr. Fang was the recipient of the Humboldt Research Fellowship, National Excellent Young Scientists (Overseas), two IEEE Prize Paper Awards, one Best Presenter Award, IEEE JOURNAL OF EMERGING AND SELECTED TOPICS IN POWER ELECTRONICSStar Reviewer Award, Chinese Government Award for Outstanding Self-Financed Students Abroad in 2018, and the Best Thesis Award from NTU in 2019. He was World's Top 2 Highly Cited Scientists ranked by Stanford University.

Xi Liu was born in Jiangxi, China, in 1995. He received the B.S. degree in automation from the Huazhong University of Science and Technology, Wuhan, China, in 2017. He is currently working toward the Ph.D. degree in electrical engineering with the School of Control Science and Engineering, Shandong University, Jinan, China.

His current research interests include multilevel inverters and renewable power generation.

Tong Liu received the B.S. degree from the Harbin University of Science and Technology, Harbin, China, in 2014, the M.S. degree in electrical engineering from the University of Dalian Jiaotong University, Dlian, China, in 2018, and the Ph.D.degree in electrical engineering from Shandong University, Jinan, China, in 2022.

Since 2023, he has been a Postdoc of the School of Electrical Engineering, Shandong University, Jinan, China. His current research interests include multilevel inverters, renewable power generation, and predictive control.

Guanguan Zhang (Member, IEEE) received the B.Sc. degree in automation and the Ph.D. degree in control science and engineering from Central South University, Changsha, China, in 2012 and 2018, respectively.

From 2016 to 2017, she was a joint Ph.D. student with the Department of Energy Technology, Aalborg University, Aalborg, Denmark, where she focused on the reliability analysis of wind power system. She is currently an Associate Research Fellow with the School of Control Science and Engineering, Shandong University, Jinan, China. Her research interests include control, applications, and reliability of power converters and renewable energy generation.

Chenghui Zhang (Fellow, IEEE) was born in Shandong Province, China, in 1963. He received the B.S. and M.S. degrees in automation engineering from the Shandong University of Technology, Jinan, China, in 1985 and 1988, respectively, and the Ph.D. degree in control theory and operational research from Shandong University, Jinan, in 2001.

In 1988, he joined Shandong University, where he is currently a Full Professor of power electronics and power drives with the School of Control Science and Engineering, and the Director of the Research Center of Power Electronics Energy-Saving Technology and Equipment of the Chinese Education Ministry. He was selected as a Changjiang Scholar of the Education Ministry in 2009, and a Taishan Scholar of Shandong Province in 2009, respectively. His research interests include optimal control of engineering, power electronics and motor drives, and energy-saving techniques.